CERN LIBRARIES, GENEVA

CM-P00044114

CERN/PSCC/89 – 11
PSCC/P117

9 March, 1989

Proposal to the PSCC

HIGH RESOLUTION SPECTROSCOPY OF X – RAYS FROM ANTIPROTONIC HYDROGEN AND HELIUM ISOTOPES USING A CRYSTAL SPECTROMETER

G.L. Borchert, D. Gotta*, O.W.B. Schult
Institut für Kernphysik, KFA Jülich
D – 5170 Jülich

L.M. Simons
PSI, CH – 5234 Villigen

K. Elsener**
Institute of Physics, University of Aarhus,
DK – 8000 Aarhus C

K. Rashid
Pakistan Institute for Nuclear Science and Technology,
Islamabad

J.J. Reidy
Physics Department, University of Mississippi,
University, Miss. 38677, USA

* Spokesman
** Contactman

ABSTRACT

A precision measurement is proposed of the line shape and energy shift of antiprotonic L_α transitions for nuclei with $A \leq 4$. These measurements study the antiproton–proton and antiproton–nuclear spin–spin and spin–orbital interaction at threshold. The high intensity LEAR beam will be stopped in the cyclotron trap. This provides an intense X–ray source at low gas pressures. A focussing crystal spectrometer will be used to measure the X–ray energies with a resolution $\Delta E/E$ of 10^{-3} to 10^{-4}. This permits for the first time a direct measurement of the strong interaction shifts and widths of the 2p levels in different antiprotonic hydrogen isotopes. Furthermore the accuracy of the present detection methods will be increased by two orders of magnitude. This should allow the resolution of fine structure and hyperfine structure in favourable cases.

CONTENTS

1 INTRODUCTION

In antiprotonic atoms the spin–spin and spin–orbital dependence of the strong interaction of the antiproton with nuclei can be studied without orienting the antiproton beam or the target. It is sufficient to observe the influence of the strong interaction as shift and broadening of atomic X–ray transitions in the fine structure or hyperfine structure separately.

The most interesting antiprotonic systems are formed with the isotopes of hydrogen and helium. A high precision experiment offers an elegant opportunity to study the isotopic and isobaric strong interaction effects by comparing with theories based on the elementary $\bar{N}N$ interaction.

Up to now only the gross features (1s global shift and width and 2p width of antiprotonic hydrogen, 2p global shift and width and 3d width of the helium isotopes [1–6]) could be extracted from the experimental results (tab. 1). Due to the limited resolution of X–ray drift chambers, gas–scintillation chambers and Si(Li)–semiconductor detectors that have been used, the complex structure of the L_α–transitions could not be resolved. As an example, the theoretically predicted level splitting of $\bar{p}H$ is shown in fig. 1. To perform a detailed study of the Balmer transitions in elements with $A \leq 4$, an increase of precision of the energy determination of more than a factor of 100 is desirable.

It is a common feature that in these atoms the yields of the Balmer series are not sensitive to the hadronic widths of the np levels [6,7], because their strong interaction widths are a factor of at least 100 larger than the el.–mag. decay widths. Due to the even larger absorption in $\bar{p}D$ and $\bar{p}T$ the observation of the respective K_α–transitions is doubtful. Thus only lower limits of the 2p–level widths can be estimated. The importance of a high resolution measurement is the possibility of measuring 2p shifts and widths directly in all the hydrogen isotopes. The resolution facilitates the discrimination of various models [8–17]. Current models typically predict the same gross shifts and widths and differ essentially in their prediction of fine and hyperfine structure (tab. 2 and fig. 2).

Finally, determination of the fine and hyperfine structure constrains the extrapolation procedures from low energy polarized scattering data (FILTEX[18]). It should be emphasized that antiprotonic 2p–states are the initial states in a number of experiments taking place at LEAR now (Crystal barrel [19], OBELIX [20]).

For a direct measurement of the 2p–level shifts and widths of the antiprotonic hydrogen isotopes and the resolution of fine and hyperfine structures, the accuracy of the energy determination must be about 10^{-4}. This can now be achieved with a crystal spectrometer. Such instruments have, however, rather low efficiency. This can be alleviated by combining the high intensity LEAR beam, the cyclotron trap (saturated yields of the X–ray transitions and a small stop volume) with a focussing crystal spectrometer in Johann geometry (spectrograhic modus). This is the approach of this proposal.

2 MOTIVATION

In antiprotonic hydrogen and helium the annihilation occurs predominantly from the 2p and 3d levels if low pressure gas targets are used as e.g. in LEAR experiment PS 175 (table 1). Although restricted to angular momentum l=1, antiprotonic atoms with $A \leq 4$ offer the possibility to study the strong interaction characterized according to spin, angular momentum and isospin.

2.1 STRONG INTERACTION

The very strong annihilation causes a strong absorption at long range, which is indicated by the participation of several partial waves even at low energies [21]. Thus the effects caused by the spin–spin and the spin–orbit interaction are usually hidden by the strong annihilation and comparison with different potential models are not very conclusive. Information on the spin–spin and the spin–orbit forces is, however, very important due to the different behaviour of the $\bar{N}N$ and the NN interaction. A comparison of the $\bar{N}N$ and NN interaction is given in [22].

Potential models usually start from (known) NN potentials, which are transformed to the $\bar{N}N$ potential by the G–parity transformation [23] or using equivalent exchange potentials [10]. The annihilation is described by a phenomenological complex potential of short range, which is required to reproduce the $\bar{p}p$–scattering data. The $|\bar{n}n>$ state is taken into account by coupled channel calculations and proper isospin mixing [10,11].

In the black–sphere model the annihilation is described by the classical mean free path of antinucleons in nuclei [10,12]. The very strong annihilation is reflected in the pathlength of only about one nucleon diameter. Predictions of the strong widths for the 2p levels of protonium include the determination of the dominant isospin contributions. The model has been applied to nuclei with $A \geq 4$ [24].

In a microscopic approach the $\bar{N}N$ interaction is derived from the annihilation and rearrangement of quarks and antiquarks [21,25]. In a pure rearrangement picture only the protonium $^1S_0$ and $^3S_1$ shifts and widths have been calculated up to now. These calculations underestimate the experimental values by a factor 2–5 [25].

A calculation performed for $\bar{p}D$ follows a multiple scattering approach [17] successfully used in pion absorption. An optical potential is constructed from a basic $\bar{N}N$ potential as given in [23]. A similar approach has been used to calculate for light nuclei the complex energy shifts of fine and hyperfine levels separately [26]. Due to the peripheral nature of the $\bar{p}A$ absorption, a comparison of the extended deuteron with the rather compact tritium or helium nuclei provides constraints for the construction of potentials tested at the outer parts of the nuclear wave functions.

Precise data can show significant deviations from the scaling of the shifts and widths based on the scattering length approximation. In this picture the lowest level is connected to higher states of same angular momentum by the radial overlap [27–30]. Using in addition the low–energy approximation of the scattering amplitudes, s– and p–state parameters are related by the (effective) annihilation radius only [27,31]. Information on the $\bar{p}n$–interaction, however, should come from the comparison of the hydrogen isotopes and the isobars ^{3}He and T. The structure of the 2p level of $\bar{p}^3$He is predicted to be completely different from that of $\bar{p}^4$He and should rather be compared with $\bar{p}$T. State–dependent absorption from the 3d level causes deviations from the statistical intensity ratios.

The 2p–level splitting of $\bar{p}$H and $\bar{p}$D is predicted to be dominated by the el.–mag. interaction (tab. 2). The calculation performed using the Dover–Richard potential [23] yields hadronic 2p shifts comparable with a calculation using π^o exchange only [8]. However, mean shifts as already measured for $\bar{p}$He are not predicted by π^o exchange indicating that at smaller distances the approximation fails.

2.2 CASCADE STUDIES

The velocity distribution of the exotic atoms causes a Doppler broadening of the X–ray lines. With a kinetic energy of 1 eV [6,7], a broadening of 52 meV occurs for the L_α transition of $\bar{p}$H, which is of the same order of magnitude as the mean hadronic broadening. As the Doppler broadening scales with X–ray energy, a different width detected in the transitions from the series limit directly yields the velocity, if a state–independent velocity distribution is assumed. A significant deviation from a thermal velocity distribution has been detected in pionic liquid hydrogen [32].

Measurements detecting the recoil neutrons of the reaction $\pi^-p \rightarrow \pi^0 n$ at rest yield two distinct distributions of the kinetic energy of the π^-p system of comparable magnitude: i) up to 1 eV and ii) a high energy tail up to 70 eV originating from Coulomb acceleration. Indications for epithermal velocities come also from myon catalyzed–fusion experiments using DT–mixtures. The exact knowledge of the Doppler broadening is essential for the interpretation of the data, especially in the case of $\bar{p}H$. This information has to be obtained from a measurement of the M transitions from the series limit (usually denoted as M_∞) of $\bar{p}D$ (E=1.85 keV). For these transitions any broadening caused by strong interaction can be neglected compared to the experimental resolution.

In $\bar{p}He$ the cascade is influenced in addition by molecule–ion formation [33]. The charged $\bar{p}He$ system is expected to be more thermalized than the neutral $\bar{p}H$ system. This assumption, however, has to be confirmed, e.g. by the measurement of the $\bar{p}He$ (5–4) transition (E=1.69 keV).

With decreasing pressure a drastic increase of the L_α yields (fig. 3) indicates dramatic changes of the population in the higher parts of the atomic cascade. The total intensity tends more and more to be shared between the circular transition ($l_{i,f}=n_{i,f}-1$) and the transitions from the series limit (L_∞). The total intensity of the unresolved L_∞ transition is about 10 % and almost constant below a few 100 mbar. To get insight into the higher parts of the cascade, individually resolved transitions from the series limit have to be measured. The highest state with orbital quantum number n, which can be resolved, is given by $n^3 = 2 \cdot n_f/(\Delta E/E)$, where n_f denotes the final state of the series considered and $\Delta E/E$ is the experimental resolution. With a resolution of $\Delta E/E = 10^{-4}$ the distribution up to n=40 should be measureable.

The collision rate and therefore the level mixing due to the Stark effect depends on the velocity of the exotic atom. The use of a cascade model [7] yields a kinetic energy of $T(\bar{p}p) = (1.0 \pm 0.3)$ eV [6]. The velocity, however, depends on the assumed Stark mixing parameter. Hence, combining the existing knowledge about the $\bar{p}H$ ($\bar{p}D$) cascade with crystal spectrometer studies of Doppler broadening will allow the determination of the velocity of the systems.

3 EXPERIMENTAL SET–UP

With the cyclotron trap using the LEAR beam, an X–ray source of high specific activity can be provided. The X–ray beam penetrating through a bore hole of the magnet is reflected by the crystal of the Johann spectrometer and will be detected by a position–sensitive detector.

Major advantages of the set–up (fig. 4) are

- the detector is not exposed directly to the source, which keeps background low, and
- all energies of the interesting energy interval are measured simultaneously using the spectrometer in Johann geometry with a position–sensitive detector (spectrographic modus).

3.1 CYCLOTRON TRAP

The principle of the cyclotron trap is the winding up of the range curve of a particle beam in a weak focussing magnetic field. The field is produced by a superconducting split coil magnet [34,35]. After injection the particles spiral towards the center while loosing energy in the target gas. The beam is stopped within a few cm^3. The antiprotons, which are captured into high atomic orbits, emit X–rays during the last steps of the atomic cascade only. The cyclotron trap will be used to achieve high yields of the Balmer transitions.

Recent experiments yield the following figures: From the 105 MeV/c LEAR beam up to 86 % of the antiprotons were stopped at a pressure of 30 mbar hydrogen (fig. 5), which is about the pressure at which we plan to work. The antiprotons were degraded to about 60 MeV/c by the 100 μm beryllium exit window of the beam tube with a diameter of 18 mm and the defining scintillator of 200 μm Ne102A (fig. 6). The dimensions of the beam spot at the window have been measured to be about 1mm x 2mm. The fine range was adjusted by interchangeable mylar foils located between the beam tube window and the scintillator. The exit window of the beam tube was flanged directly to the target chamber as close as possible to the defining scintillator to prevent the beam from being

analyzed in the inhomogeneous magnetic field.

The radial and axial distribution of the antiproton stops have been determined with the help of intensity measurements of antiprotonic nitrogen X–rays. The radial distribution has been measured directly using collimators at z=70 mm and a Si(Li)–detector placed at z=350 mm (z is the coordinate along the symmetry axis of the magnetic field); the distribution was found to extend ~ 30 mm (FWHM). The axial distribution has been obtained by pushing a cylinder step by step towards the center of the trap and measuring the decrease of intensity with a Si(Li) detector. Because the cylinder disturbs the deceleration of the antiprotons, only an upper limit of the extension of about 50 mm (FWHM) could be obtained.

Because the extension of the stop distribution is essentially determined by the betatron amplitudes excited during the injection into the trap, a 30 μm beryllium window with a diameter of 4 mm only is foreseen in the proposed experiment. Together with a correspondingly smaller scintillator and degrader, this window allows injection with smaller betatron amplitudes. A stop distribution of 12 mm diameter (FWHM) can then be expected. This yields an improvement of 10^5 in the stop density compared to a linear device.

Discussion of the $\bar{p}$T–experiment will be based on the experience of a first hydrogen measurement. For the tritium measurement a tight inner chamber with welded beryllium windows of 100 μm for the beam and 25 μm for the X–rays will be used. At low gas pressures the activity would be only 400 Ci.

3.2 CRYSTAL DIFFRACTOMETER

The Bragg spectrometer consists of a crystal arrangement and a position–sensitive detector mounted on a precise support (fig. 4). The Bragg angle corresponding to the energy of the reflected X–rays is given by half the angle between the two arms and is measured by a high precision encoder with 1" ($5 \cdot 10^{-6}$) accuracy. The focal length of the crystals is chosen between 3 to 5.6 m, which is the optimum for the planned experiment. To minimize absorption losses on the photon paths, the target volume is directly connected via vacuum–tight tubes with a chamber containing the crystals and further flanged to a chamber containing the position–sensitive detector.

3.2.1 BRAGG CRYSTAL

The reflection crystal must be bent to cylindrical shape. Different techniques to curve the crystal plates have been tested: Generally we use either a precisely shaped steel block to glue the crystals onto it or two of such blocks for clamping. Because the energies to be studied range from 1.7 to 14 keV and the reflection properties vary strongly with photon energy, different types of crystals have been or are being tested (tab. 3). To further increase the angular acceptance, an array of individually adjusted crystals is being prepared.

The calculated values of the reflecting power R_I given in table 3 for energies of 1.7–2.6 keV, however, are not achievable in practice when larger and curved crystals are used. Deviations of up to one order of magnitude must be expected as can be seen in table 3 for the crystals already tested in the 11 keV region.

The size of the X–ray source and the spatial resolution of the detector require a focal length of $R = 3 - 5$ m. To achieve sufficient counting rates, crystal areas of 100–200 cm^2 will be used. The horizontal (x) and vertical (y) dimensions of the crystal cause a defocussing $\propto R^{-2}$ on the order of 10^{-5} at energies around 2 keV and of 10^{-4} around 11 keV. The vertical defocussing can be corrected to order $(y/R)^2$ using the two–dimensional information of the detector. The Johann broadening due to the horizontal extension can be diminished considerably using a special shaping of the crystals (Johansson type crystals [38]).

3.2.2 POSITION–SENSITIVE DETECTOR

A multi–wire proportional chamber (MWPC) is used as position–sensitive detector. The vertex in two dimensions is determined by the center of gravity of the charge influenced on the x and y cathodes. As gas filling mixtures of Xe/CH_4 and Ar/C_2H_6 (90%/10%) are used.

According to the maximum size of the crystals, a sensitive area of 25 cm height and 8–10 cm width is foreseen for the detector. The parameters of the MWPCs are given in table 4.

In addition a silicon micro–strip detector with 125 μm wide strips is being considered for measurements in the 11 keV range.

3.2.3 DATA ACQUISITION

Each cathode channel of the MWPC is equipped with a separate preamplifier and shaping amplifier connected to a fast encoding CAMAC ADC system (FERA). The anode signal is used after fast shaping and pulse height discrimination to trigger the anode and all cathode ADCs. The data are stored event by event in a fast ECL–memory unit. The slowly shaped anode signals are used for pulse shape analysis. Full buffers are transferred to a micro–VAX and processed at low priority. This procedure permits an on–line control of data taking. Refined cuts can be applied in the off–line analysis for further background reduction.

3.3 TEST OF PERFORMANCE

The crystal spectrometer has been tested off–line in the KFA Jülich. A Se target at the position of the cyclotron trap source has been photo excited by means of an X–ray tube. The emitted K_α X–rays correspond in energy rather precisely to the $\bar{p}^4$He L_α X–rays. A prototype LiF(400) crystal of 5cm x 10 cm with a radius of curvature of 3.7 m (see table 3) was used to reflect the photons and to focus them onto a MWPC with an active area of 10 cm x 10 cm. A typical spectrum is shown in fig. 7. Since the spatial resolution of the MWPC in this energy region corresponded to 2 eV, the natural X–ray line width being 3 eV, the registered line width is determined essentially by the reflection width of the LiF crystal. This width amounts to 70 seconds of arc corresponding to 6 eV. An absolute intensity calibration by means of a Si(Li) detector yields a peak reflectivity of (6±2)% for LiF(400).

In fig. 8a the energy resolution of the MWPC is shown in the energy range of a ^{55}Fe source and the 11.2 keV K_α–radiation of Se. The efficiency was measured with calibrated sources and using the X–ray fluorescence method. The spatial resolution of the MWPC was tested separately by using a collimated 50 μm wide X–ray beam from a

^{55}Fe source. A series of positions was measured controlled by means of a micrometer screw. A typical resolution of 250 μm FWHM has been achieved with an Ar/C_2H_6 gas filling at 2 bar (fig. 8b). This corresponds to a geometrical resolution of $\Delta E = 1.9$ eV in the focal region for the above mentioned LiF(400) reflection.

3.4 BACKGROUND

The background consists of $\bar{p}$ induced events and a constant rate from the radioactivity of the surrounding materials and from cosmic rays.

The beam induced background is prompt. It originates to 85 % from annihilations in the gas (see fig. 5). To estimate an upper limit for the rate, we assume that the X–rays emerging from the center of the cyclotron trap through the windows of the target chamber are scattered isotropically by the crystal and reach the detector from there. Consequently this background intensity is proportional to the product of the solid angle of the crystal and of the detector relative to the crystal. All other directions are shielded by the magnet, its iron return yoke and the detector shield.

To estimate this annihilation background experimentally, a measurement with the 10 cm x 10 cm MWPC (filled with a Xe/CH_4 mixture at 2 bars) has been performed at LEAR. The MWPC was placed behind a window of the target chamber at a distance of 86 cm from the center of the cyclotron trap. A total number of 2130 X–rays (about 70/s) per 10^6 incoming antiprotons was detected in the energy interval from 9–13 keV. This number reduces to $806/10^6\bar{p}$, when a valid x–y information of the MWPC is required. From this experiment an upper limit of 44 events per 10^9 incoming antiprotons is derived. This limit assumes a 12 cm x 10 cm crystal set–up at a Bragg angle $\Theta_B = 30^o$, a focal length of 4 m and a MWPC of 10 cm x 25 cm sensitive area. A more realistic estimate, which takes into account only coherently scattered X–rays implies a reduction of the background rate by another factor of 10.

The beam–independent background stems from radiation of radioactive contaminations in and outside the MWPC and from interactions of cosmic rays and plasma discharges of the MWPC. A total trigger rate of 22/s was measured in the LEAR M1 area with the 10 cm x 10 cm MWPC. Appropriate setting of the thresholds of the anode

and cathodes and limitation of the cluster size reduced the rate to 1–2 /s within a 4 keV energy window around 11 keV. A further reduction of 50% was obtained by installing 5 cm thick iron plates between the MWPC and the surrounding concrete walls. Thus, we expect a maximum beam–independent background of 0.5/s with a passive shielding in a 10 cm x 10 cm MWPC similar to the rates obtained in the Jülich laboratory.

According to the discussion above the beam–independent background dominates. Hence, the total background is proportional to the measuring time. Both the beam–dependent and the beam–independent backgrounds were measured to be uniform over the sensitive area of the detector. The background determining the peak to background ratio reduces by the ratio of the area covered by the reflection to the total area. For the LiF(400) reflection of the 11 keV X–rays, e.g., 1 eV corresponds to 0.11 mm. In this case the background rate amounts to 5 events per hour and eV in a MWPC of 25cm height.

A further reduction is feasible using an active shield around the detector and placing two additional wire planes behind the x cathode acting as a charged particle VETO. A pulse shape analysis of the anode pulses is foreseen to exclude triggers originating from discharges. The time resolution of the MWPC of less than 100 ns allows for the correlation of the antiproton annihilation with the detection of the X–rays.

3.5 CALIBRATION

The off–line calibration of the spectrometer is performed with fluorescence X–rays. An X–ray tube is flanged radially to the target chamber irradiating interchangeable target materials placed at the center of the trap. At a radial distence of $\sim$ 60 cm the X–ray tube can be shielded from the magnetic field allowing for short term calibrations. The intensity of this radiation is monitored by a Si(Li) detector.

For energy calibration in the energy range considered the following fluorescence X–rays can be used [39]. The value for copper is taken from [40].

Si	$K_{\alpha 1}$: E = (1740.012 ± 0.013) eV	dE/E =	$8 \cdot 10^{-6}$
S	$K_{\alpha 1}$: E = (2307.882 ± 0.030) eV	dE/E =	$13 \cdot 10^{-6}$
Cl	$K_{\alpha 1}$: E = (2622.428 ± 0.056) eV	dE/E =	$21 \cdot 10^{-6}$
Cu	$K_{\alpha 1}$: E = (8047.865 ± 0.008) eV	dE/E =	$2 \cdot 10^{-6}$
As	$K_{\alpha 1}$: E = (10543.86 ± 0.09) eV	dE/E =	$9 \cdot 10^{-6}$
Se	$K_{\alpha 1}$: E = (11222.53 ± 0.20) eV	dE/E =	$18 \cdot 10^{-6}$

The measurement of the X–rays of $\bar{p}$He(5–4),$\bar{p}$O(7–6),$\bar{p}$Ne(8–7) or $\bar{p}$Ar(12–11) at equivalent gas pressures provides a calibration under beam–on conditions with equal stop distributions for all elements. The yields of the antiprotonic X–ray transitions are saturated and not affected by the strong interaction. The natural line width is negligible compared to the experimental resolution.

The precision of calculated el.–mag transition energies [41] is expected to be of the order of a few eV. We will test the calculations to a few tenth of an eV and determine whether the QED problem of the $\bar{p}$A atom is understood up to this level.

3.6 SYSTEMATIC ERRORS

As the crystal is coupled thermally to the support of the spectrometer, short term variations of the temperature are avoided. In addition, a tent will prevent cooling by air currents. With these precautions the change of the lattice constant due to thermal extension can be neglected. Moreover, the energy calibration will be checked every few hours.

The most prominent contaminations of the target gas are nitrogen and oxygen with a relative concentration of about 10^{-4}. Except for very rare cases, the crystal itself provides the energy discrimination. The transitions $\bar{p}$Ar(12–11) and $\bar{p}$O(7–6) coincide with the antiprotonic L_α transition of the helium isotopes within a few eV. The helium transitions are broadened to several eV, whereas the contamination lines exhibit the experimental resolution.

The target chamber produces only aluminum fluorescence X–rays due to the aluminum coating of the chamber materials. Contamination originating from the MWPC itself can be detected by long term background measurements and contributions from fluorescence X–rays by irradiation with, e.g., a ^{60}Co–source.

The angular encoders of the spectrometer are controlled on–line. Thus the position of the crystal and the detector will be stabilized to the intrinsic accuracy of the encoders.

3.7 COUNTING RATES AND PRECISION

The number n of X–rays detected is given by

$$n = N_{\bar{p}} \cdot f_{stop} \cdot Y \cdot \epsilon_D \cdot \{(\Delta\Omega/4\pi) \cdot P \cdot (\Delta Q/Q)\}$$

with

- $N_{\bar{p}}$ = no. of incoming antiprotons
- f_{stop} = the stop efficiency of the cyclotron trap
- Y = yield of the X–ray transition
- ϵ_D = efficiency of the detector.

The expression in curly brackets determines the properties of the crystal set–up:

- $\Delta\Omega$ = solid angle of the reflecting crystal area
- P = peak–reflectivity ($\simeq R_I/\Delta\Theta$)
- $\Delta Q/Q$ = fraction of source accepted by the crystal

The attenuation of the X–rays in the tubes filled with the target gas can be neglected for the low pressure used.

In table 5, estimates of the count rates for selected crystals are given per 10^{10} antiprotons entering the cyclotron trap. In some cases a crystal of good resolution and fairly large acceptance is compared to a quartz crystal, which usually yields the ultimate resolution, but modest reflectivity. The rate estimates are based on a stop distribution of 12 mm diameter (FWHM), a stop efficiency of 0.8 and a 10 cm x 10 cm crystal area. Yields and detection efficiencies are the same as given in table 1 and table 4.

The rates derived from the calculated integrated reflectivity R_I assuming an ideal mosaic crystal are too optimistic by a factor of about 5. This is demonstrated by the comparison of the theoretical and measured integrated reflectivity as shown in table 3 for the test crystals in the 11 keV region. The rate estimates for the $\bar{p}$He experiment are based on the data obtained in the performance tests, which are expected to represent rather a lower than an upper limit. Using curved crystals, variations of 50% for the reflectivity are not unusual for probes of identical materials.

The background estimates, derived from the test measurement described in sec. 3.4 are given in table 6 together with the results of Monte–Carlo simulations of the line–shapes (fig. 9). The rates are taken from the last column of table 5, the shifts and widths from theoretical predictions (tab. 2) or experimental information, if available (tab. 1). The intensity ratios are assumed to be statistical and the background to be flat. All fits start with the pattern of the pure el.–mag. splitting. The intensity ratios are fixed.

In all cases the mean values of shift and width could be determined to high accuracy (tab. 6 and fig. 10). A complete resolution of all hyperfine components is feasible for $\bar{p}$H, if the ultimate resolution of 50 meV is reached (fig. 9a). For deuterium (fig. 9b) and the helium isotopes (fig. 9c,d) the hadronic broadening exceeds the experimental resolution. Mean values of subgroups could be derived for $\bar{p}$D. The widths are, however, overestimated due to the coupling to the el.–mag. pattern. For $\bar{p}^4$He the fine structure components are resolved, if the splitting exceeds 20 eV.

The monitoring detector consists of an array of 4 Si(Li) detectors of 80 mm^2 each, which can sustain high counting rates. It can be used during the measuring periods for high statistics studies of the $\bar{p}$H K_α transitions. The purpose of these studies will be to resolve the singlet ($^1S_0$) and triplet ($^3S_1$) hyperfine components of the ground state.

4 ADDITIONAL MEASUREMENTS

4.1 BY–PRODUCTS OF USING THE BRAGG–SPECTROMETER

- Using the calibration lines mentioned in sec. 3.6, the X–ray energies can be determined with an accuracy of up to a few 10^{-6}. Measuring transitions not affected by strong interaction would test the calculations of the el.–mag. energy levels in a regime where the contributions due to finite size [41] and polarizability [42] are negligible – they are of the order of 10^{-7} to 10^{-6} – and electron screening is absent.
- The precision of the calculation without finite size and polarization effects exceeds the one of the calibration, which hence determines the precision of the antiproton mass. Masses of nuclei are known to a much higher accuracy than the calibrations used here [43].
- Electronic transitions in antiprotonic argon, krypton and xenon have been observed [44]. From the splitting of the electronic transitions, the state of the electron shell is determined for a stage when the antiproton is still in the higher part of its cascade. The analysis of these states is envailed by the insufficient resolution of the Si(Li)–detectors used up to now.

4.2 OUTLOOK

The use of crystal spectrometers permits the determination of other quantities. However, such studies are not part of the present proposal and will thus be mentioned only briefly.

With the low–energy spectrometer proposed for the hydrogen and helium experiments, X–rays up to 20 keV can be measured. A DuMond spectrometer such as the one used at ISOLDE [45] is suitable for energies between 30 and 100 keV. For such measurements solid targets will be used. Then the following experiments become feasible:

- measurement of the fine structure splitting to a precision of $\Delta\mu/\mu=10^{-3}$ for the magnetic moment $\mu(\bar{p})$ of the antiproton. This requires an energy resolution of at least $\Delta E/E=10^{-4}$, which can hardly be achieved at low energies

around 10 keV. With a DuMond spectrometer, however, resolutions of 10^{-4} can be reached. Similar conditions arise for the strong interaction effects in FS splitting [46,47]. A small coupling to 2^+ nuclear states [48] and a minimal correction due to electron screening [41] should be combined.

- measurement of the reduced mass of the $\bar{p}$A–system, e.g., $\bar{p}^{208}$Pb(15–14). This mass can be determined up to the limit given by the X–ray energy standard [49,50].
- measurement of a shift due to nuclear and antiproton polarization. The relative shift reaches a few 10^{-5} of the transition energy (e.g. $\bar{p}^{208}$Pb(15–14), E=110 keV). In the two examples above again the effect of electron screening has to be considered.
- direct measurement of upper widths of last observable transitions (e.g. $\bar{p}$Be(4–3), E=17 keV).
- the search for a degeneration of the energy levels of the $\bar{p}$A–system and an electron in a 1s level with respect to the $\bar{p}$A system would allow a very precise measurement of el.–mag. properties due to the small width of the levels (e.g. eKr(np–1s) <–> $\bar{p}$Kr(n–>n–1)).

5 REQUEST

5.1 BEAM PARAMETERS

A small stop distribution requires a stable focus. For this reason the beam position must be kept within 1 mm and the distance of the cyclotron trap to the last quadrupole must be less than 2 m.

- beam momentum : 105 MeV/c, $\Delta p/p \leq 10^{-3}$
- emittance: $\leq 20\ \pi$ mm mrad (V), $\leq 10\ \pi$ mm mrad (H)
- low–energy beam line with stabilized beam elements
- spill length optimized to supress non–correlated background

The following numbers of antiprotons needed have been estimated:

- $\bar{p}^3$He (3–2) and $\bar{p}^4$He (3–2) : $5 \cdot 10^{11}\,\bar{p}$
- $\bar{p}$H (3–2) and $\bar{p}$H (∞ –2) : $8 \cdot 10^{11}\,\bar{p}$
- $\bar{p}$D (3–2) and $\bar{p}$D (∞ –2) : $8 \cdot 10^{11}\,\bar{p}$

In order to keep systematic errors small, a total consumption of $2–4 \cdot 10^{10}$ antiprotons per day would be desirable.

5.2 SPACE REQUIREMENTS

The angular range to be covered by the spectrometer requires a free space of 5 m perpendicular to the beam direction and 4 m in the beam direction near to the cyclotron trap (see fig. 11). The support of the spectrometer (about 2000 kg) must be installed in a way to keep the plane of the Rowland circle in position when the Bragg angle or the focal length is changed. Therefore the precision rails carrying the support have to be attached to the floor.

Additional requirements are:

- Access to the area with LN_2– and LHe–vessels for the superconducting magnet
- a climatized hut of about 30 m^2 for the electronics
- the space for a tent covering the spectrometer and attached to the magnet to prevent short term temperature variations caused by current of air.

5.3 TIME SCHEDULE

A set–up time of 3 months is envisaged to begin in autumn 1989. A test beam time of 1 – 2 weeks should take place at the end of 1989. Only low intensities would be needed. Afterwards typical running periods of 3–4 weeks would be preferred. The spectrometer must be installed at least two weeks before the measurement so that it can be adjusted and thermally stabilized.

The first step is the measurement of the helium isotopes since the requirements concerning beam consumption and calibration are less stringent. The hydrogen and the helium experiments require a considerable change of the crystal set–up and the Bragg angle, i.e. the movement of the spectrometer support and appropriate calibrations.

6 REFERENCES

1. J.D. Davies, T.P. Gorringe, J. Lowe, J.M. Nelson, S.M. Playfer, G.J. Pyle, G.T.A. Squier, C.A. Baker, C.J. Batty, S.A. Clark, S. Sakamoto, R.E. Welsh, R.G. Winter, E.W.A. Lingemann, PL 145B(1984)319

2. C.A. Baker, C.J. Batty, S.A. Clark, J. Moir, S. Sakamoto, J.D. Davies, J. Lowe, J.M. Nelson, G.J. Pyle, A. Selvarajah, G.T.A. Squier, R.E. Welsh, R.G. Winter, E.W.A. Lingeman, C.W.E. van Eijk, R.W. Hollander, D. Langerveld, W.J.C. Okx, A. Zoutendijk, NP A483(1988)631

3. C.W.E. van Eijk, R.W. Hollander, D. Langerveld, W.J.C. Okx, A. Zoutendijk, R. Feirreira–Marques, C.A. Baker, C.J. Batty, S.A. Clark, J. Moir, S. Sakamoto, J.D. Davies, J. Lowe, J.M. Nelson, G.J. Pyle, G.T.A. Squier, R.E. Welsh, R.G. Winter, E.W.A. Lingeman, NP A486(1988)604

4. M. Ziegler, S. Ahmad, C. Amsler, R. Armenteros, E.G. Auld, D. Axen, D. Bailey, S. Barlag, G. Beer, J.C. Bizot, M. Botlo, M. Comyn, W. Dahme, B. Delcourt, M. Doser, K.D. Duch, K. Erdmann, F. Feld–Dahme, U. Gastaldi, M. Heel, B. Howard, R. Howard, J. Jeanjean, H. Kalinowsky, F. Kayser, E. Klempt, C. Laa, R. Landua, G. Marshall, H. Nguyen, N. Prevot, J. Riedlberger, R. Rieger, L. Robertson, C. Sabev, U. Schaefer, O. Schreiber, U. Straumann, P. Truöl, H. Vonach, P. Weidenauer, B.L. White and W.R. Wodrich, PL 206B(1988)151

5. R. Bacher, P. Blüm, J. Egger, K. Elsener, D. Gotta, K. Heitlinger, W. Kunold, D. Rohmann, M. Schneider and L.M. Simons, Proc. ANTIPROTON 86 (Thessaloniki) eds. S. Charalambous, C. Papastefanou and P. Pavlopoulos (World Scientific, Singapore, 1987) p. 223

6. R. Bacher, P. Blüm, D. Gotta, K. Heitlinger, D. Rohmann, M. Schneider, J. Egger, L.M. Simons and K. Elsener, to be published

7. E. Borie and M. Leon, PR A 21 (1980) 1460

8. S. Barmo, H. Pilkuhn and H.G. Schlaile, Z.f.Phys. A301(1981)283

9. E. Borie, Z.f.Phys. A278(1976)127

10. W.B. Kaufmann and H. Pilkuhn, PR C 17(1978)251

11. J.M. Richard and M.E. Sainio, PL 110B(1982)349

12. W.B. Kaufmann, PR C 19(1979)440

13. B. Moussallam, Z.f.Phys. A325(1986)1

14. A.M. Green and S. Wycech, NP A377(1982)441

15. W. Schweiger, J. Haidenbauer and W. Plessas, PR C 32 (1985) 1261

16. R.H. Landau and J. Schnick, PR C 36 (1987) 1942

17. S. Wycech, A.M. Green and J.A. Niskanen, PL 152B(1985)308

18. Contributions to the Proc. of the IV. LEAR workshop Villars–sur–Ollon, 1987 (Harwood Academic, Chur 1988), p. 183–224 and p. 313

19. CRYSTAL BARREL Collaboration, CERN/PSCC/85–56 (1985) and ibidem p. 493, 503

20. OBELIX Collaboration, CERN/PSCC/85–76 (1985)

21. A.M. Green and J.M. Niskanen, Progress in Part. and Nucl. Physics, ed. A. Faessler, vol. 18 (1987), p. 93

22. W.W. Buck, C.B. Dover and J.M. Richard, Ann. of Phys. (NY) 121(1979)47

23. C.B. Dover and J.M. Richard, PR C 121(1980)1466

24. W.B. Kaufmann and H. Pilkuhn, PL 166B(1986)279

25. G. Ihle, H.J. Pirner and J.M. Richard, PL 183B(1987)15

26. O. Dumbrajs, H. Heiselberg, A.S. Jensen, A. Miranda, G.C. Oades and J.M. Richard, NP A457(1986)491

27. I.S. Shapiro, Phys. Rep. 35(1978)129

28. V.E. Markushin, preprint ITEP–65 (1980)

29. V.S. Popov, A.E. Kurdryavtsev, V.I. Lisin and V.D. Mur, Zh. Eksp. Teor. Fiz. 80(1981) 1271

30. O.D. Dalkarov, B.O. Kerbikov and V.E. Markushin, Yad.Fiz. 25(1977)853

31. T.L. Trueman, NP 26(1961)57

32. J.F. Crawford, M. Daum, R. Frosch, B. Jost, P.–R. Kettle, R.M. Marshall, B.K. Wright and K.O.H. Ziock, PL B213(1988)391

33. F. Reifenröther, E. Klempt and R. Landua, Proc. of the IV. LEAR workshop Villars–sur–Ollon, 1987 (Harwood Academic, Chur 1988), p. 733

34. L.M. Simons, R. Bacher, P. Blüm, D. Gotta, W. Kunold and M. Schneider, THE CYCLOTRON TRAP: A Device To Produce High Stopping Densities of Exotic Atoms, in preparation

35. L.M. Simons, Physica scripta T22(1988)90

36. W.H. Zachariasen, "The Theory of X–ray diffraction in Crystals", Wiley, New York, 1945

37. A.J. Burek, in Workshop on X–ray Instrumentation for Synchrotron Radiation research, eds. H. Winick and G. Brown, SSRL Report No. 78/04(1978)III–8

38. T. Johansson, Z. Physik 82(1933)507

39. J.A. Bearden, Rev. of Mod. Phys. 39(1967)78

40. E.G. Kessler, R.D. Deslattes and A. Henins, PR A19(1979)215

41. E. Borie and B. Jödicke, computer code PBAR, KfK internal report 14.02.01.P11C (1985) and B. Jödicke, Diploma work, KfK report no. 3933 (1985)

42. T.E.O. Ericson and J. Hüfner, NP B47(1972)205

43. A.H. Wapstra and K. Bos, At. Data and Nucl. Data Tables 19(1977)175

44. R. Bacher, P. Blüm, D. Gotta, K. Heitlinger, M. Schneider, J. Missimer, L.M. Simons and K. Elsener, PR A 38(1988)4395

45. G.L. Borchert, P.G. Hansen, B. Jonson, H.L. Ravn, O.W.B. Schult and P. Tidemand–Petersson, NIM 178(1980)209

46. A. Kreissl, A.D. Hancock, H. Koch, Th. Köhler, H. Poth, U. Raich, D. Rohmann, A. Wolf, L. Tauscher, A. Nilsson, M. Suffert, M. Chardalas, S. Dedoussis, H. Daniel, T. von Egidy, F.J. Hartmann, W. Kanert, H. Plendl, G. Schmidt and J.J. Reidy, Z. f. Phys. A329(1988)235

47. E. Borie, PR A28(1983)855

48. A.M. Green, G.Q. Liu and S. Wycech, NP A483(1988)619

49. R.D. Deslattes and E.G. Kessler: Experimental Evaluation of Inner–Vacancy Level Energies for Comparison with Theory, from ATOMIC INNER–SHELL PROCESSES, ed. by B. Craseman (Plenum Publishing Corporation, 1985), p. 191

50. E.G. Kessler, R.D. Deslattes, A. Henins and W.C. Sander, PRL 40(1978)171

7 TABLES

	NUCLEUS		$E(L_\alpha)$	ϵ_{2p}	Γ_{2p}	Γ_{3d}	p	$Y(L_\alpha)$	$Y(L_{tot})$	$Y(M_{tot})$	A(3d)
	I	T	/keV	/meV	/meV	/μeV	/mbar	%	%	%	%
H	1/2	1/2	1.737	–	32±10	–	16	52±11	71±12	44b	0.5
D	1	0	2.317	–	>100a	50±17	16	25± 5	35± 5	44b	22
T	1/2	1/2	2.605	–	–	–					
			/keV	/eV	/eV	/meV					
^{3}He	1/2	1/2	10.440	–17±4	25± 8	2.1±0.2	72	26± 4	33± 8	64±11	26±4
^{4}He	0	0	11.129	–18±2	46± 5	2.3±0.1	72	21± 3	33± 7	57± 6	22±2

Table 1: Mean values of the el.–magn. L_α–transition energies [8,9] and experimental information on yields, strong shifts and widths of antiprotonic hydrogen and helium isotopes from experiment PS 175 [5,6] unless indicated otherwise (a:[3],b:from a cascade calculation using the parameters fitted to the results of PS 175). The fraction of antiprotons annihilating from the 2p level is practically equal to the total yield of the Balmer series. A(3d) is the fraction of annihilations from the 3d level.

	r_2 /fm	Γ^X_{2p} /meV	HFS/FS	el–mag. HFS/FS /meV	hadronic $\epsilon_{2p}/\Gamma_{2p}$ /meV						
$\bar{p}$H	230	0,38	2^3P_2 2^3P_1 2^1P_1 2^3P_0	+ 60 − 16 ± 0 −249 [8]	+ 5/45 +25/32 −25/29 −25/194 [10]	− 5/30 36/20 −26/26 −74/112 [11]	−/− +35/16 −28/14 −69/118 [12]	− 3/28 +32/19 −30/28 −72/112 [13]	− 5/32 +37/24 −29/26 −84/130 [14]	15/20 38/26 2/26 13/50 [15]	−/24 [16]
$\bar{p}$D	173	0.51	$2^2P_{1/2}$ $2^2P_{3/2}$ $2^4P_{1/2}$ $2^4P_{3/2}$ $2^4P_{5/2}$	+376 −338 −398 +170 +51 [8]	70/398 67/386 63/512 45/430 44/420 [17]						
$\bar{p}$T	154	0.57	see $\bar{p}$H	–	−/−						
$\bar{p}^3$He	77	34	2^3P_2 2^3P_1 2^1P_1 2^3P_0	−1200* −6219* +4415* +2930* [8]	−/−						
$\bar{p}^4$He	73	35	$2\ p_{1/2}$ $2\ p_{3/2}$	+2710 −1355	−7/36 eV −6/38 eV [26]	−/42eV [24]					

Table 2: Predictions for the hadronic 2p–level fine and hyperfine splitting and broadening ($\epsilon_{2p}/\Gamma_{2p}$) of antiprotonic hydrogen and helium.
The el.–mag. HFS/FS shifts are the splitting relative to the mean el.–mag. binding energies including vacuum polarization [8]. r_2 is the 2p–Bohr radius and Γ^X_{2p} the el.–mag. decay width. The "el.–mag." shifts of $\bar{p}^3$He include π^o–exchange [8].

Energy /keV	wavelength /Å	crystal plane		Θ_B	$R_I \cdot 10^{-5}$	$\Delta\Theta$	ΔE /eV
1.736	7.146	ADP	101	42° 6'27"	4.4	9"	0.24
		ADP	200	71°37'33"	25	50"	0.19
		PET	002	54°50'55"	11	21"	0.66
		EddT	020	54°12'	8	16"	–
		Quartz	100	57° 6'19"	5	10"	0.05
2.317	5.351	Si	111	58°34'46"	10	21"	0.18
		Quartz	100	38°57'30"	1.1	2"	0.11
		ADP	101	30° 8'20"	3	6"	0.40
		Eddt	020	37°25'	5	10"	–
2.605	4.760	Si	111	49°22'40"	6	12"	0.21
		Quartz	100	34° 0'12"	2	4"	0.17
		ADP	101	26°31'30"	4	8"	0.35
		EddT	020	32°48'	5	10"	–
11.129	1.141	* LiF	400	33°33'56"	2.0	70"	6
		LiF	400		14	30"	2.5
		* Si	333	32°12'42"	0.4	90"	8
		Si	333		3.5	7"	0.6
		* Si	400	24°12'42"	3.7	120"	15
		Si	400		14	30"	3.6
		* Si	440	35°28' 4"	1	110"	8
		Si	440		5.4	11"	0.9

Table 3: Crystal properties. The integrated reflectivity R_I corresponding to an angular acceptance $\Delta\Theta$ are taken for an ideal mosaic crystal [36,37]. The energy resolution has been calculated using the Darwin–Prins model including absorption [37]. At 11 keV measurements were performed using a photo–excited Se–target to determine reflectivity and resolution experimentally (*). The precision is about 30 %. Similar differences as for the prototype crystals used at 11 keV are expected also in the energy region of 1.7 – 2.6 keV.

gasfilling	window	pressure /bar	ΔE/E %	Δx /mm	at E /keV	ϵ_D %	at E /keV
Ar/C_2H_6	12 μm mylar	1	35		1.7	32a	1.7
		1	25		5.4	14±5b	5.4
Xe/CH_4	12 μm mylar	1				62a	2.3
		1				72a	2.6
Xe/CH_4	1 mm Be	2	18	0.2	5.9	53±5	6.4
						40±5	14.4
						68a	11.2
						41a	14.4

Table 4: Set–up parameters of the MWPC.
The measurements of energy–, position–resolution Δx (FWHM) and efficiency ϵ_D using calibrated sources were performed for a prototype MWPC of 10cm x 10cm sensitive area.
a – calculated efficiencies (a transmission of 80% for the wire mesh supporting the mylar foil is assumed).
b – the wire mesh used for the prototype MWPC has a transmission of only 40%.

	energy /keV	crystal plane		P_{th} %	P_{exp} %	$\Delta Q/Q$ %	$N(L_\alpha)_{exp}$ $/10^{10}\ \bar{p}$
$\bar{p}H$	1.736	ADP	101	30	5	5.6	800
		Quartz	100	60	10	0.8	140
$\bar{p}D$	2.317	Si	111	75	15	1.6	300
		Quartz	100	45	9	1.3	210
$\bar{p}T$	2.605	Si	111	74	15	0.9	220a
$\bar{p}He$	11.129	Si	400	40	6*	4.4	800
		LiF	400	63	6*	6.1	600

Table 5: Estimated total intensity recorded in a MWPC for L_α transitions for selected crystals.

P_{th}: Peak reflectivity calculated for an ideal mosaic crystal

P_{exp}: Expected or measured (*) peak reflectivity

$\Delta Q/Q$: Fraction of the source intensity used within one FWHM of the resolution of the crystal.

a – The same X–ray yield as for $\bar{p}D$ is used.

$\bar{p}$H(3–2)	MC–input			fit		MC–input	fit	
	ϵ_{2p}^{tot} /meV	Γ_{2p} /meV	Int	ϵ_{2p}^{tot} /meV	Γ_{2p} /meV	Int	ϵ_{2p}^{tot} /meV	Γ_{2p} /meV
$^3P_2$	+55	30	10000			2500	54±4	27±8
$^3P_1$	+29	20	6000	–23±1	23±5	1500	10±5 – –23±1	40±30 – 28±3
$^1P_1$	–26	26	6000			1500	–21±8	19±10
$^3P_0$	–323	112	2000	–321±8	57±27	500	–321±16	103±31
Ref.	[8,11]	[11]						
ΔE/meV			200			50		
$N_{\bar{p}}$			$4\cdot10^{11}$			$3.8\cdot10^{11}$		
BG/5meV			50			100		
S/BG			1.87			0.82		

$\bar{p}$D(3–2)	MC–input			fit	
	ϵ_{2p}^{tot} /meV	Γ_{2p} /meV	Int	ϵ_{2p}^{tot} /meV	Γ_{2p} /meV
$^2P_{1/2}$	+446	398	1000	400±105	
$^2P_{3/2}$	–271	386	2000	–235±40	430±165
				–275±35	
$^4P_{1/2}$	–335	512	1000	–250±90	
$^4P_{3/2}$	+215	430	2000	160±50 – 170±25	– 685±95
$^4P_{5/2}$	+ 95	420	3000	90±25	
				–36±1	493±48
Ref.	[8,17]	[17]			
ΔE/meV			200		
$N_{\bar{p}}$			$3\cdot10^{11}$		
BG/5meV			80		
S/BG			0.24		

Table 6: Results of Monte–Carlo simulations of the line–shape of L_α transitions.

The intensities are assumed to be statistical.
ΔE: experimental resolution
$N_{\bar{p}}$: number of incoming antiprotons
BG: background/channel
S/BG: signal to background ratio (ratio of the peak intensity (area) to the background intensity (area) over an interval of 5 FWHM of the peak)

$\bar{p}^3$He(3–2)	MC–input			fit		MC–input	fit	
	ΔE^{HFS} /eV	Γ_{2p} /eV	Int	ΔE^{HFS} /eV	Γ_{2p} /eV	Int	ΔE^{HFS} /eV	Γ_{2p} /eV
$^3P_2$	–1.2	25	6000			6000		
$^3P_2$	–6.2	25	3600	–1.2±0.2	25±0.6	3600	–0.6±0.3	25.2±1.0
$^1P_1$	+4.5	25	3600			3600		
$^3P_0$	+2.9	25	1200			1200		
Ref.	[8]	[5]						
ΔE/eV			6			6		
$N_{\bar{p}}$			$2.1 \cdot 10^{11}$			$2.1 \cdot 10^{11}$		
BG/0.5eV			50			250		
S/BG			1.1			0.22		

$\bar{p}^4$He(3–2)	MC–input			fit		MC–input	fit	
	ΔE^{FS} /eV	Γ_{2p} /eV	Int	ΔE^{FS} /eV	Γ_{2p} /eV	Int	ΔE^{FS} /eV	Γ_{2p} /eV
$^2p_{1/2}$	2.70	46	5000	0.2±0.4	46.5±1.7	5000	0.1±0.7	47.8±2.1
$^2p_{3/2}$	–1.35	46	10000			10000		
Ref.	[8]	[5]						
$^2p_{1/2}$	+10	46	5000	10±2	46±2			
$^2p_{3/2}$	–10	46	10000	10±1	48±5			
ΔE/eV			6			6		
$N_{\bar{p}}$			$2.8 \cdot 10^{11}$			$2.8 \cdot 10^{11}$		
BG/0.5eV			50			250		
S/BG			0.45			0.09		

Table 6: cont.

8 FIGURES

Fig. 1: Scheme of the low–lying levels of antiprotonic hydrogen.
Splittings and widths are taken from [8,10 and 11]. Experimentally determined global 1s shift and width are taken from [3].

Fig. 2: Theoretical predictions of the 2p–level total shift and strong interaction widths for A≤4 (KP:[24], D:[26] and table 2). The experimental information from PS 174 and PS 175 is included (a:[6], b:[2], c[3]). For the helium isotopes the pure el.–mag. hyperfine and fine structure ist marked.

Fig. 3: Pressure dependence of the yields of the Balmer transitions of antiprotonic hydrogen. The data from experiment PS 175 [6] are compared to a cascade calculation [7].

Fig. 4: Cross–section fo the experimental set–up for a Bragg angle Θ_B=30°.
a – beam tube with appendix for the target chamber
b – stop distribution (X–ray source)
c – monitor detector
d – support for the spectrometer arms (e)
f – vacuum tight tube

Fig. 5: Time distribution of the antiproton stops in the cyclotron trap. At 30 mbar H_2 86% of the 105 MeV/c beam could be stopped in the gas in the center of the target chamber.

Fig. 6: Cross–section of the target chamber showing the extended beam tube, the degrader and the defining scintillator S.

Fig. 7: Se K_α dublet (11.181 and 11.222 keV) measured via the LiF(400) reflection (focal length R=3.76 m)

Fig. 8: a) Energy spectrum of the ^{55}Fe source and the Se K_α radiation measured with the MWPC (Xe/CH_4 at 2bar).
b) Position resolution of the MWPC measured with the beam of the ^{55}Fe source collimated to a slit of 50 μm (Ar/C_2H_6 at 2 bar; 1 channel corresponds to 50 μm).

Fig. 9: Monte–Carlo simulations of the line shape of the L_α transitions of

a) $\bar{p}H$ b) $\bar{p}D$ c) $\bar{p}^3He$ d) $\bar{p}^4He$

The input parameters and results of the analysis are given in table 6.

Fig. 10: Bounderies obtained from the statistical analysis of the Monte–Carlo simulations.

Boundaries of substructures of $\bar{p}H$, $\bar{p}D$: (– –)

Mean values: $\bar{p}H$, $\bar{p}D$ (▚), $\bar{p}He$ (– · –)

a – mean value for $\bar{p}H$ $^3P_2$, $^3P_1$ and $^1P_1$

A relative systematic error of 10^{-5} according to calibration uncertainties is marked by two legs.

Fig. 11: Floor set–up of the cyclotron trap and the Bragg spectrometer for a focal length of R=4m. The positions of crystal (a), support (b) and detector (c) move in the range of Θ_B= 20°–75° (A–C) for the Bragg angle as indicated by the dashed curves. In addition to the extreme positions the set–up for Θ_B=45° (B) is sketched.

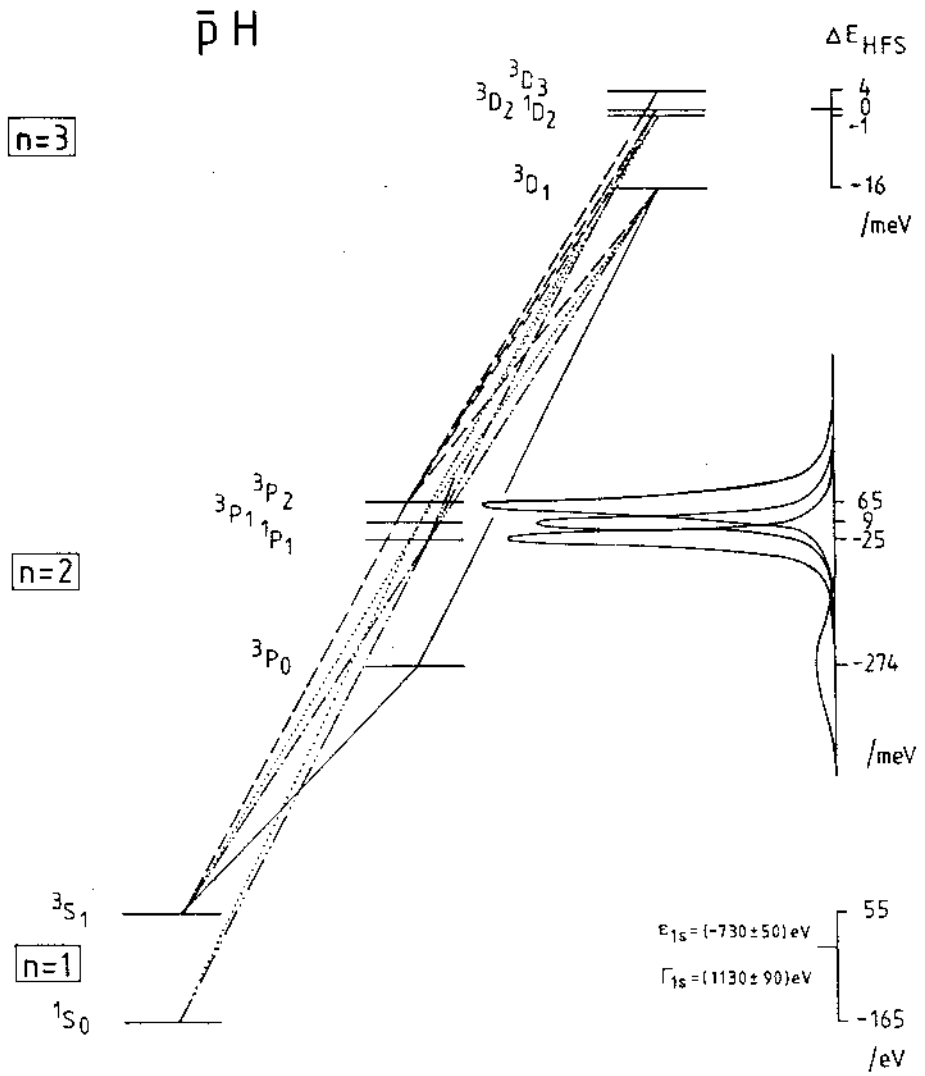
p̄ H
ΔE HFS
n=3
n=2
n=1
3D3
3D2 1D2
3D1
3P2
3P1 1P1
3P0
3S1
1S0
4
0
-1
-16
/meV
65
9
-25
-274
/meV
55
-165
/eV
ε1s = (-730 ± 50) eV
Γ1s = (1130 ± 90) eV

Fig. 1

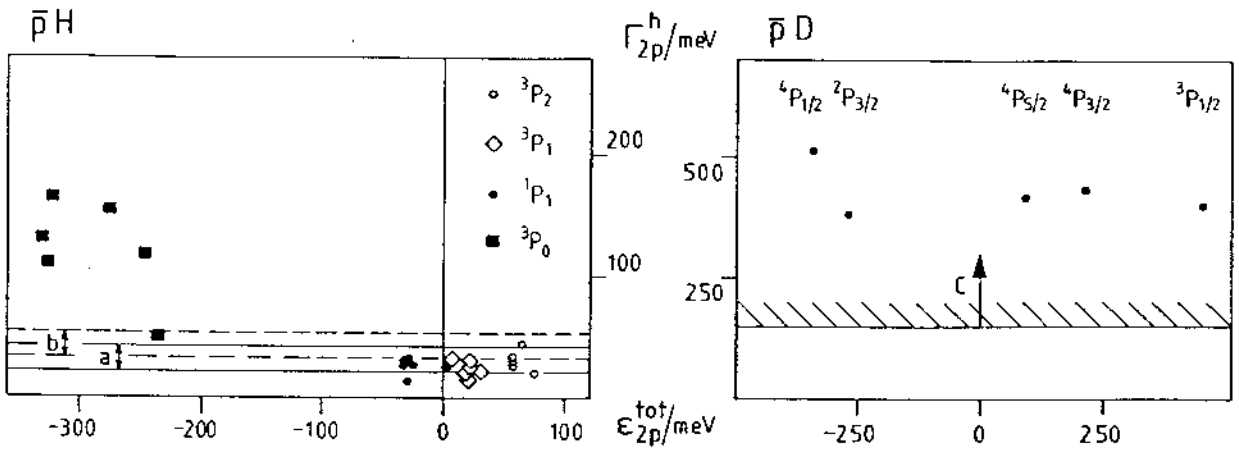
p̄ H
Γ^h_{2p}/meV
p̄ D
$^3P_2$
$^3P_1$
$^1P_1$
$^3P_0$
200
100
b
a
$^4P_{1/2}$ $^2P_{3/2}$
$^4P_{5/2}$ $^4P_{3/2}$
$^3P_{1/2}$
500
250
C
-300
-200
-100
0
100
ε^{tot}_{2p}/meV
-250
0
250

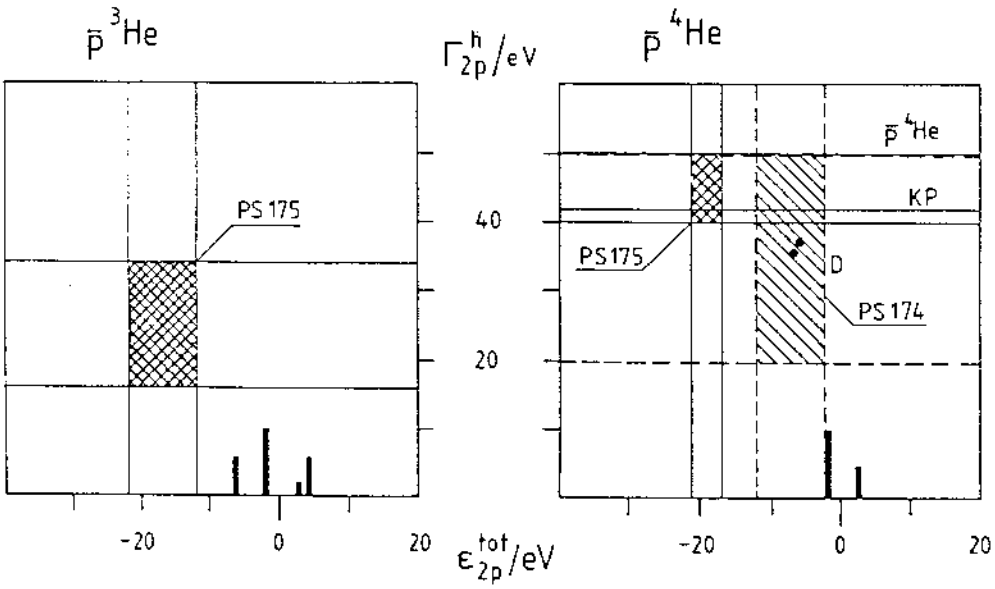
p̄ ^{3}He
Γ^h_{2p}/eV
p̄ ^{4}He
PS 175
40
20
p̄ ^{4}He
KP
PS175
D
PS 174
-20
0
20
ε^{tot}_{2p}/eV

Fig. 2

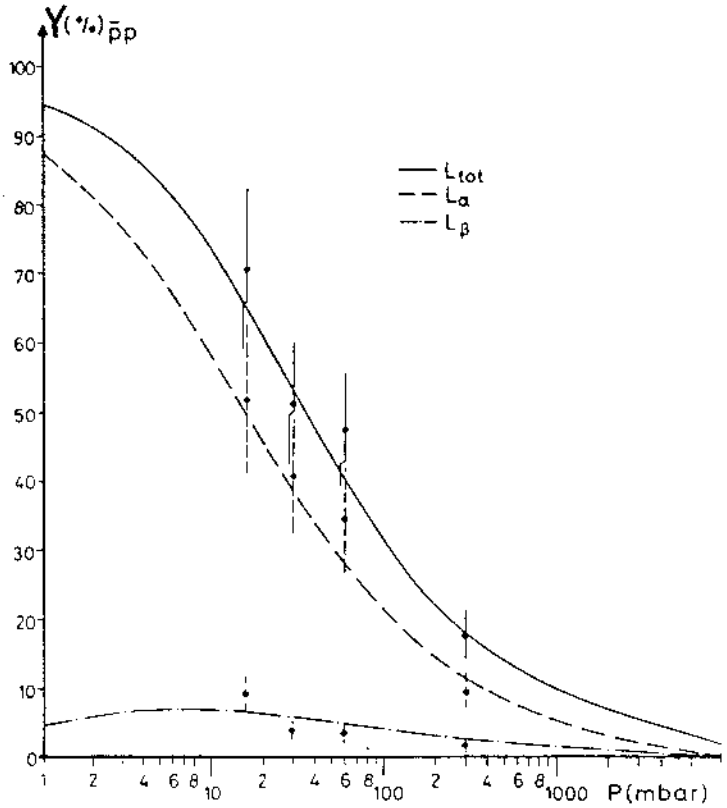
Y(%)p̄p
100
90
80
70
60
50
40
30
20
10
0
L tot
L α
L β
1
2
4
6
8
10
2
4
6
8
100
2
4
6
8
1000
P(mbar)

Fig. 3

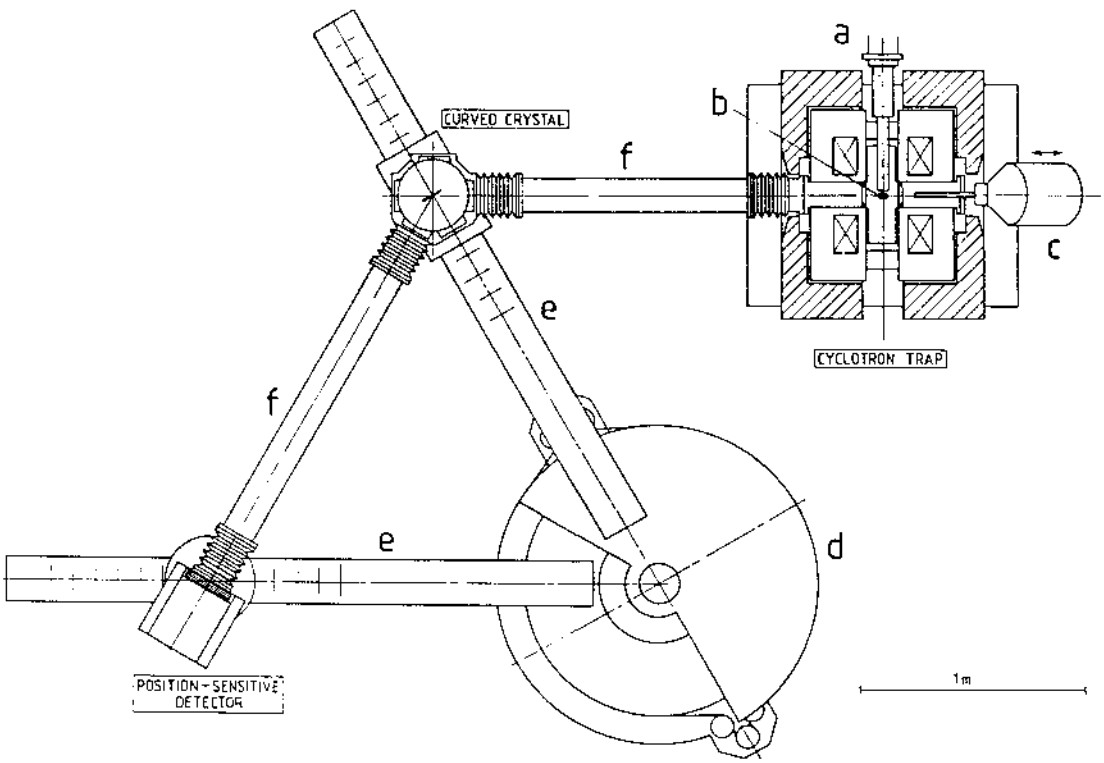
a
b
CURVED CRYSTAL
f
c
e
CYCLOTRON TRAP
f
e
d
POSITION-SENSITIVE DETECTOR
1m

Fig. 4

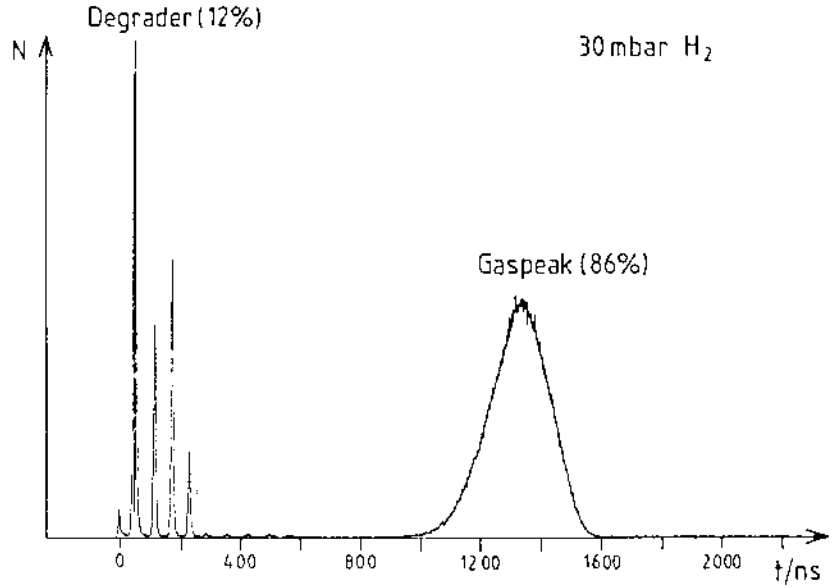
Degrader (12%)
N
30 mbar H_2
Gaspeak (86%)
0
400
800
1200
1600
2000
t/ns

Fig. 5

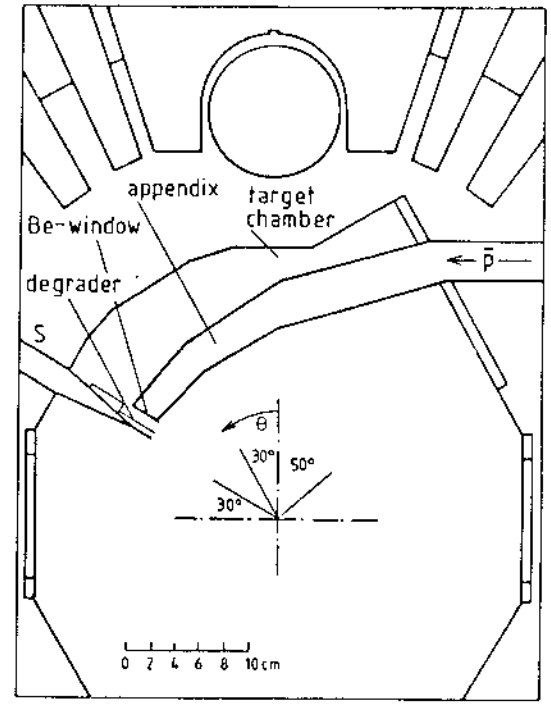
appendix
target chamber
Be-window
degrader
S
$\bar{p}$
θ
30°
50°
30°
0 2 4 6 8 10 cm

Fig. 6

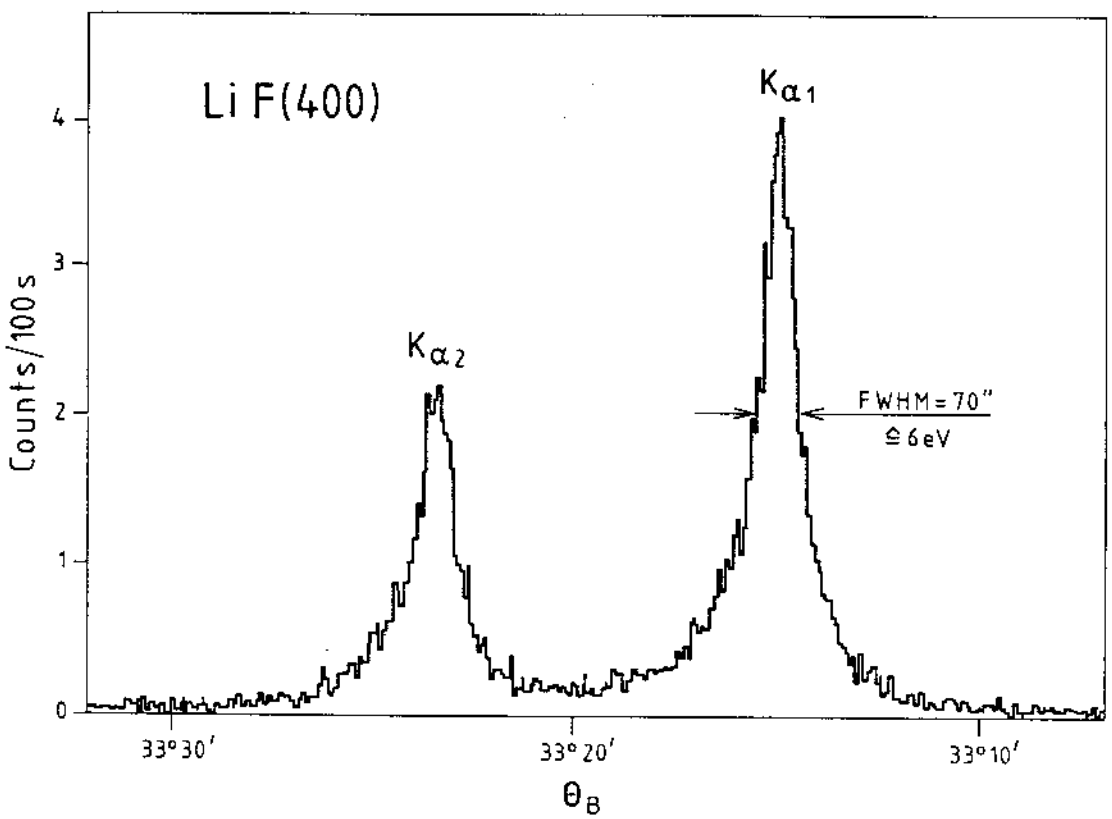
Li F(400)
Kα1
Kα2
FWHM = 70"
≙ 6 eV
Counts/100 s
0
1
2
3
4
33°30′
33°20′
33°10′
θB

Fig. 7

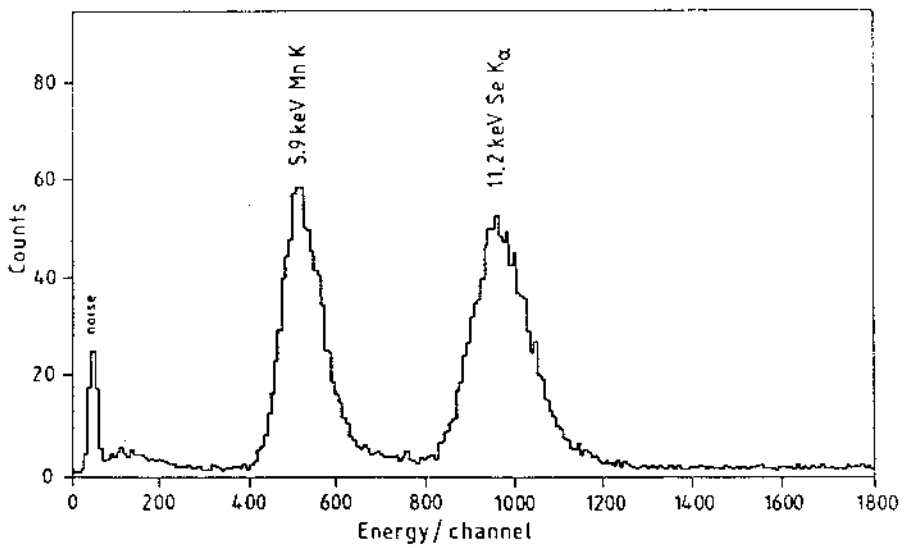
Counts
80
60
40
20
0
noise
5.9 keV Mn K
11.2 keV Se Kα
0
200
400
600
800
1000
1200
1400
1600
1800
Energy / channel

Fig. 8a

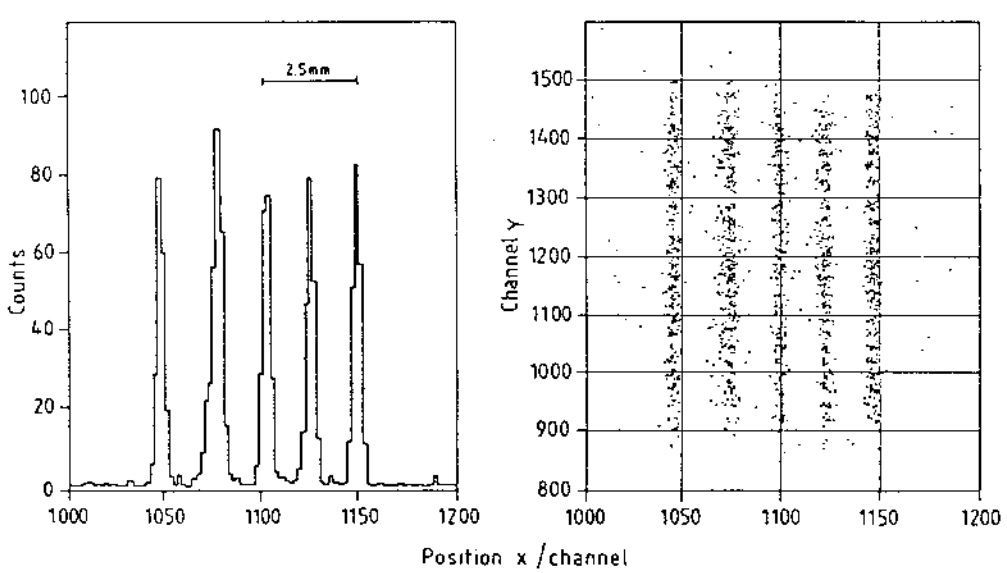
2.5mm
Counts
100
80
60
40
20
0
1000
1050
1100
1150
1200
Channel Y
1500
1400
1300
1200
1100
1000
900
800
Position x / channel

Fig. 8b

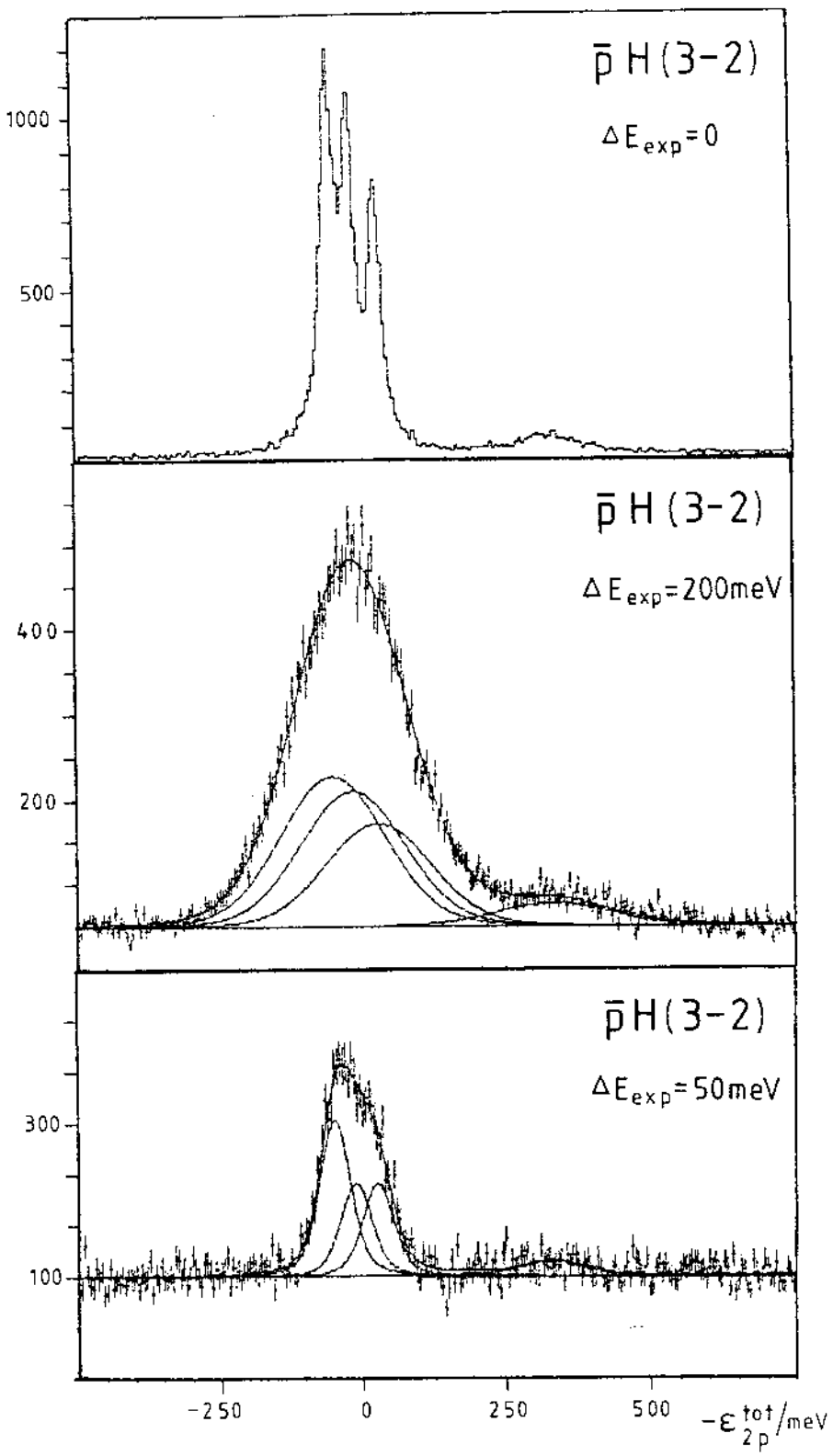
p̄ H (3-2)
ΔE_exp = 0
1000
500
p̄ H (3-2)
ΔE_exp = 200meV
400
200
p̄H(3-2)
ΔE_exp = 50meV
300
100
-250
0
250
500
-ε^tot_2p/meV

Fig. 9a

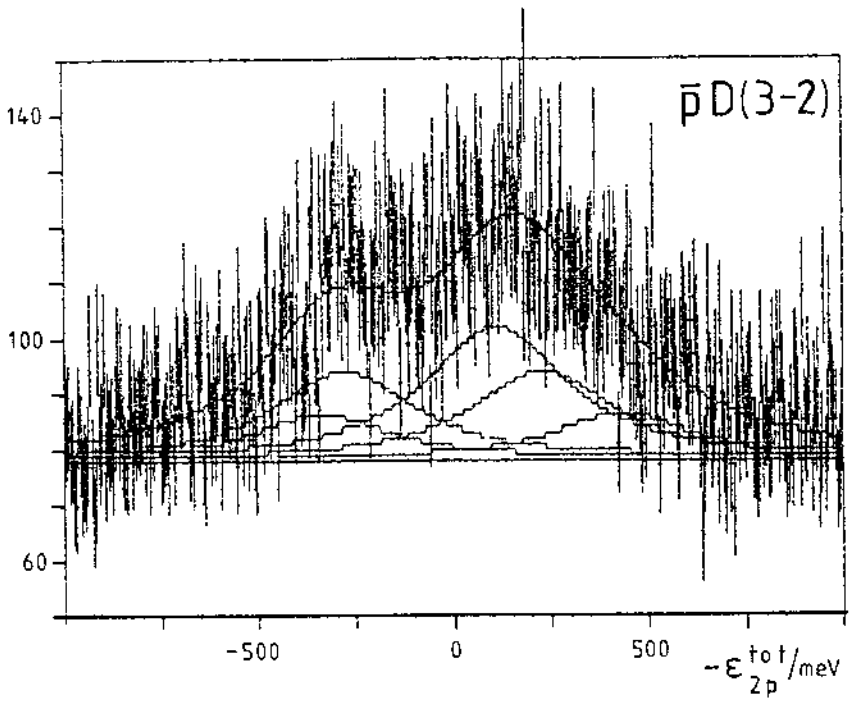
$\bar{p}D(3-2)$
140
100
60
-500
0
500
$-\varepsilon_{2p}^{tot}/meV$

Fig. 9b

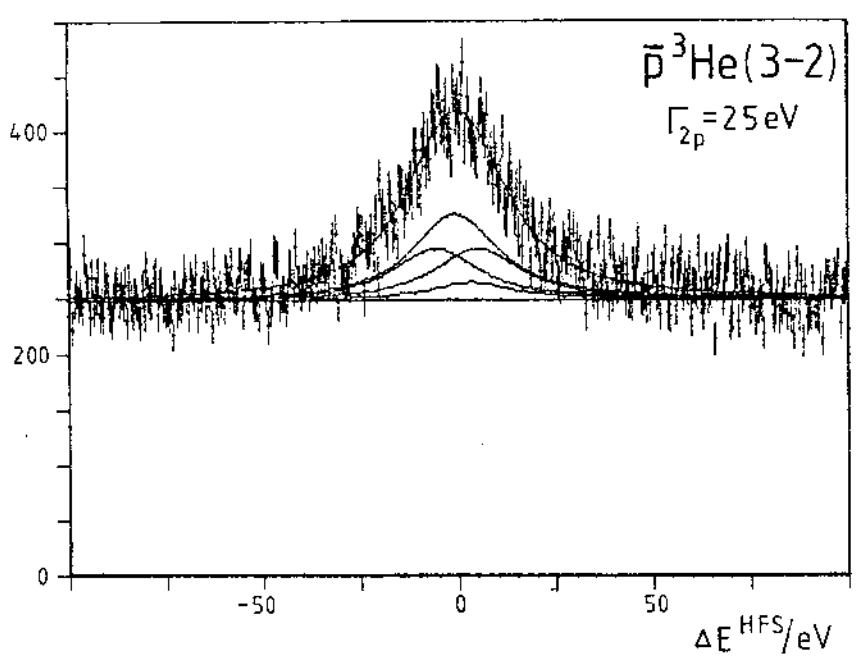
$\bar{p}^3He(3-2)$
$\Gamma_{2p}=25eV$
400
200
0
-50
0
50
$\Delta E^{HFS}/eV$

Fig. 9c

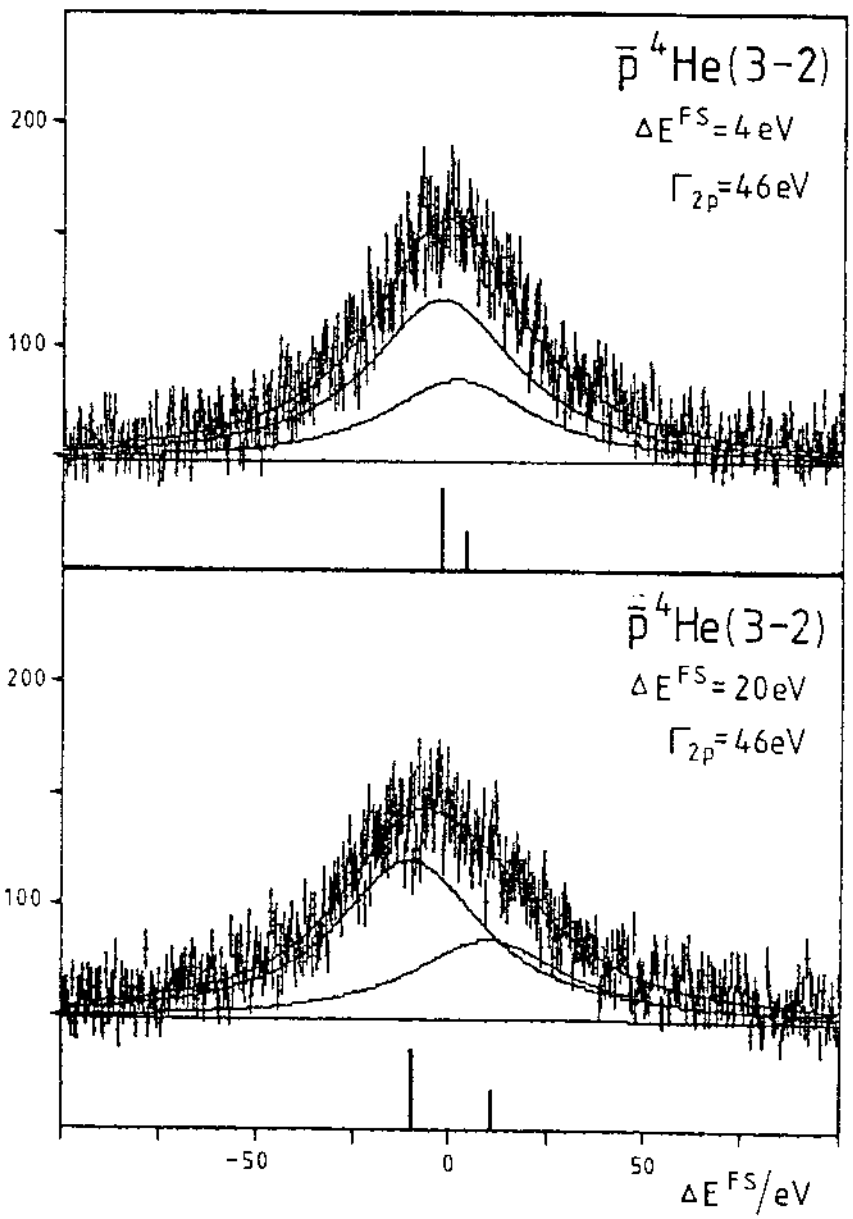
$\bar{p}\,^4He(3-2)$
$\Delta E^{FS}=4\,eV$
$\Gamma_{2p}=46\,eV$
200
100
$\bar{p}\,^4He(3-2)$
$\Delta E^{FS}=20\,eV$
$\Gamma_{2p}=46\,eV$
200
100
-50
0
50
$\Delta E^{FS}/eV$

Fig. 9d

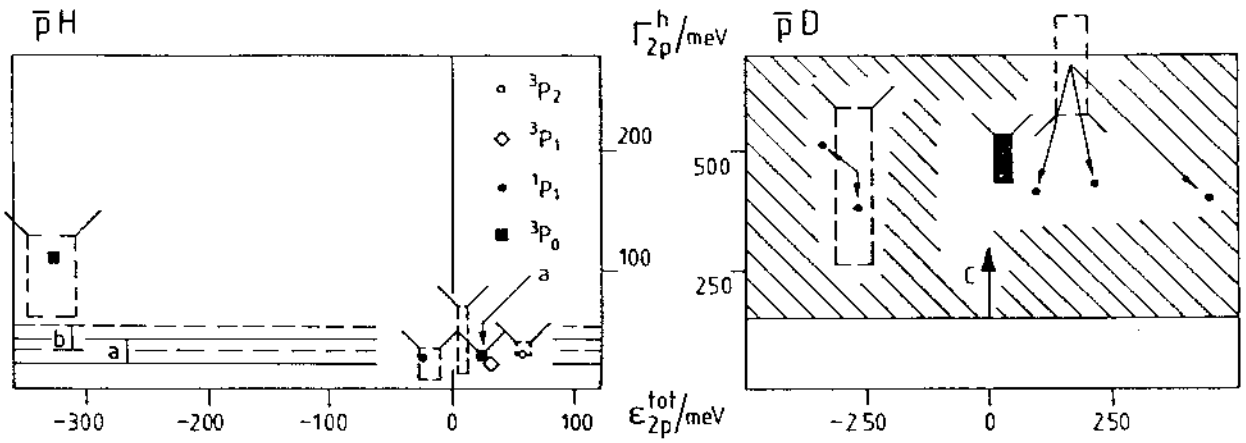
p̄ H
Γ^h_2p/meV
p̄ D
$^3P_2$
$^3P_1$
$^1P_1$
$^3P_0$
200
100
500
250
a
b
a
C
-300
-200
-100
0
100
ε^tot_2p/meV
-250
0
250

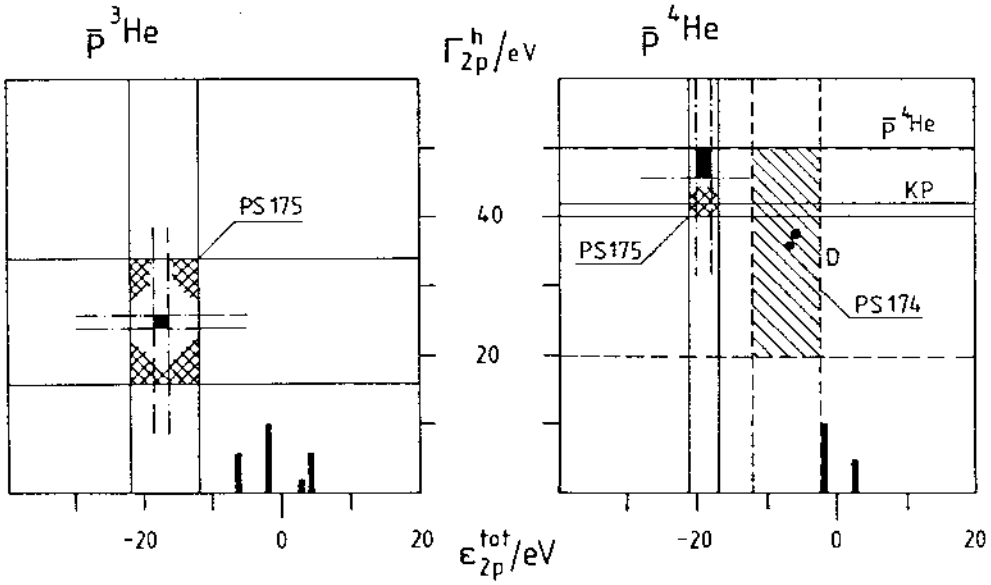
p̄ ^{3}He
Γ^h_2p/eV
p̄ ^{4}He
PS175
40
20
p̄ ^{4}He
KP
PS175
D
PS174
-20
0
20
ε^tot_2p/eV
-20
0
20

Fig. 10

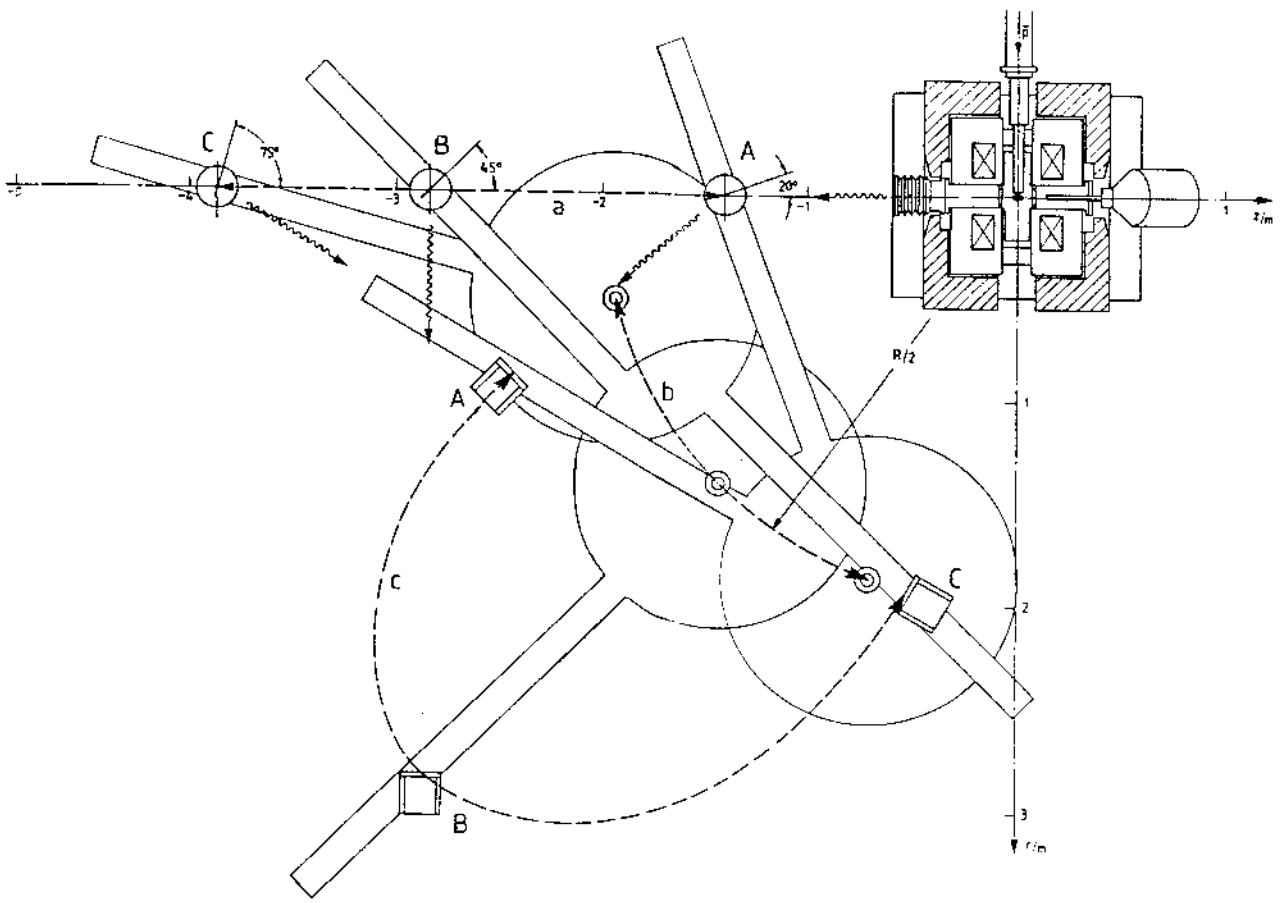

Fig. 11